Master's Thesis

Alterations in filamin mutations fine tune muscle protein aggregates

Kerttu Kotala

University of Jyväskylä

Department of Biological and Environmental Science

2 May 2024

UNIVERSITY OF JYVÄSKYLÄ, Faculty of Mathematics and Science
Department of Biological and Environmental Science
Master's Degree Programme in Cell and Molecular Biology

Kotala, Kerttu A. E.	Alterations in filamin mutations fine tune muscle protein aggregates
MSci Thesis	18 p., 2 appendices (10 p.)
Supervisors:	Professor Jari Ylänne MSc Riku Korkiamäki
Reviewers:	Professor Janne Ihalainen PhD Cornelia Böhm
May 2024	

Keywords: cheerio, *Drosophila melanogaster*, myofibrillar myopathy

Myofibrillar myopathies are genetically inherited, incurable muscle disorders which cause progressive muscle weakness in skeletal muscles. A subtype of myofibrillar myopathy called filaminopathy is caused by aggregation of filamin C and actin in the sarcomeric structures of skeletal muscle fibers. In this Pro Gradu, the aggregation of filamin was investigated in the indirect flight muscles of *Drosophila melanogaster* by expressing an open conformation mutation separately in one domain pair and two domain pairs. The mutations were located in the mechanosensory region of filamin and they were assumed to open the structure of the domain pairs. I found that single-open mutation resulted in less aggregates than double-open mutation. However, single-open aggregates were larger and less round than double-open aggregates. Also, single-open aggregates located in muscle fiber Z-disc structures whereas double-open aggregates located in between myofibrils. Upon time, single-open aggregates' volume increased, and shape developed to rounder. These findings suggest that, firstly, an open conformation mutation in one domain pair is enough for aggregate formation. Secondly, differing mutations might affect the localization of forming aggregates during tissue development. And finally, the localization of aggregates restricts the shape development of the aggregates. These detailed findings were partly unexpected and shed light on mechanisms of sarcomeric protein aggregate formation and clearance in muscle.

JYVÄSKYLÄN YLIOPISTO, Matemaattis-luonnontieteellinen tiedekunta
Bio- ja ympäristötieteiden laitos
Solu- ja molekyylibiologian maisteriohjelma

Kotala, Kerttu A. E.	Muutokset filamiinimutaatioissa hienosäätelevät lihasproteiinikasaumia
Pro gradu tutkielma:	18 s., 2 liitettä (10 s.)
Työn ohjaajat:	Professori Jari Ylänne FM Riku Korkiamäki
Tarkastajat:	Professori Janne Ihalainen FT Cornelia Böhm
Toukokuukuu 2024	

Hakusanat: cheerio, *Drosophila melanogaster,* myofibrillaarinen myopatia

Myofibrillaariset myopatiat ovat geneettisesti periytyviä, parantumattomia lihassairauksia, jotka aiheuttavat progressiivista lihasheikkoutta luustolihaksissa. Myofibrillaarisen myopatian alatyyppi filaminopatia aiheutuu filamiini C:n ja aktiinin kasautumisesta luustolihassäikeiden sarkomeerirakenteisiin. Tässä Pro Gradu -tutkielmassa filamiinin kasautumista tutkittiin *Drosophila melanogaster* kärpäsen epäsuorissa lentolihaksissa filamiinin yhden domeeniparin sekä kahden domeeniparin avoimella mutaatiolla. Mutaatiot sijaitsivat filamiinin mekanosensorisella alueella ja niiden oletettiin avaavan domeeniparien rakenteen. Havaitsin, että yhden domeeniparin avoin mutaatio tuotti vähemmän proteiinikasaumia kuin kahden domeeniparin avoin mutaatio. Tilavuudeltaan yhden domeeniparin mutaation aiheuttamat kasaumat olivat kuitenkin suurempia ja ympärysmuodoiltaan epätasaisempia kuin kahden domeeniparin mutaation aiheuttamat kasaumat. Ne myös sijaitsivat myofibrillien Z-levyrakenteissa, kun taas kahden domeeniparin mutaation kasaumat sijaitsivat myofibrillien välissä. Ajan myötä yhden domeeniparin mutaation aiheuttamien kasaumien tilavuus kasvoi ja pinnanmuoto muuttui pyöreämmäksi. Nämä havainnot osoittavat, että konformaatiomuutos yhdessä domeeniparissa on riittävä kasaumien muodostumiseen. Lisäksi filamiinin erilaiset mutaatiot näyttävät vaikuttavan muodostuvien kertymien sijoittumiseen lihaskudoksen kehityksen aikana. Kertymien sijoittuminen rakenteiden eri osiin myös rajoittaa niiden muodon kehittymistä. Nämä yksityiskohtaiset löydöt olivat osin odottamattomia ja valaisevat sarkomeeristen proteiinikasaumien muodostumis- ja poistomekanismeja lihaksessa.

TABLE OF CONTENTS

TERMS AND ABBREVIATIONS

Terms

Cheerio	Filamin C ortholog in *Drosophila melanogaster*
Double-open	An open conformation in two domain pairs
Filamin C	Actin crosslinking protein in humans
Myofibrillar myopathy	A group of muscular dystrophies caused by degradation and accumulation of Z-disc proteins or myofibrillar degradation products
Protein aggregate	A cluster of abnormally folded proteins
Single-open	An open conformation in one domain pair

Abbreviations

ABD	actin binding domain
mGFP	monomeric green fluorescent protein
Ig-like	immunoglobulin-like
MFM	myofibrillar myopathy
ROI	region of interest
WT	wild type

1 INTRODUCTION

1.1 Myofibrillar myopathies

In 1996, Nakano et al. proposed a term for muscle diseases caused by myofibrillar degradation and the accumulation of the degradation products. The new term was called myofibrillar myopathy (MFM). MFMs are genetically inherited muscle diseases that cause muscle weakness in different muscle groups. The muscle weakness is a result of focal dissolution of myofibrils and disorganization of the Z-disc structure of a sarcomere (Nakano et al. 1996). Thus far, eight different types of MFMs have been recognized (reviewed in Olivé et al. 2013). Each MFM expresses different pathological mechanisms as they are caused by mutations at different Z-disc linked proteins (e.g., desmin, titin, ZASP, and filamin).

One of the recognized MFMs is filaminopathy which, as its name suggests, is caused by the protein filamin C. Filaminopathy is a progressive muscle disease affecting either proximal leg muscles or distal upper limb muscles (Vorgerd et al. 2005, Dalkilic et al. 2006). There are three classes of pathomechanisms recognized in filaminopathy: (i) expression of misfolded filamin C which in the long run overstains natural protein degradation pathways, (ii) alteration of ligand binding properties leading to toxic gain of function, and (iii) haploinsufficiency caused by a premature stop codon (Fürst et al. 2013). Only the first pathomechanism class leads to protein aggregation which can be used in the clinical diagnosis of filaminopathy (Fürst et al. 2013).

1.1.1 Protein aggregation occurs through various pathways

In normal cell function, proteins are produced through transcription, translation, and proper folding. Errors in the folding process result in mis- or unfolded proteins and further in the formation of protein aggregates. A newly formed protein aggregate can be defined as any protein species in its non-native state so that its size is at least twice the size of the native protein (Wang et al. 2010). Multiple different factors can affect the aggregation (Wang et al. 2010). Intrinsic factors affecting the aggregation are the primary, secondary, tertiary, and quaternary structures of the protein. Extrinsic factors affecting the aggregation, on the other hand, are the environmental conditions in which the protein is present. Protein aggregation is however protein-dependent, and thus same factors might affect different proteins completely oppositely. Hence, universal rules for prevention or inhibition of protein aggregation have not yet been defined (Singh et al. 2009).

Majority of aggregation kinetics begin with the formation of aggregation nucleus followed by the growth of aggregate size (Wang et al. 2010). The form of

the aggregate, which can vary from fibril to particulate, skin, or gel, depends on the aggregation pathway (Giurleo et al. 2008). There are three major aggregation pathways which are all based on the natural folding of the amino acid chain (Wang et al. 2010). (i) In aggregation through unfolding intermediates and unfolded states, poorly populated folding or unfolding intermediates function as precursors of the aggregation process as these expose more hydrophobic patches. Completely folded or unfolded proteins, on the other hand, have their hydrophobic regions completely hidden or widely scattered and thus do not aggregate easily. (ii) In aggregation through protein self-association or chemical linkages, proteins self-associate to already existing protein aggregates through electrostatic interactions, both electrostatic and hydrophobic interactions, or only through weaker forces, such as van der Waals forces. (iii) The third protein aggregation pathway is aggregation through chemical degradations. Disulfide bond is the most common direct chemical linkage leading to protein aggregation. Other linkages are formaldehyde-mediated cross-linking, dityrosine formation, oxidation, and Maillard type reactions. Large number of surface-located cysteines can predispose to this type of aggregation. Aggregation of proteins may result as reduced or no biological activity of the cell, potential for immunogenicity, or other side effects, such as disorganization of Z-discs in MFMs.

1.1.2 Aggregate clearance mechanisms are part of normal muscle cell maintenance

Aggregated proteins alongside with misfolded proteins, overly produced proteins, or currently not needed proteins are continuously broken down into amino acids through proteolysis in normal muscle maintenance. There are two main pathways to breakdown protein aggregates. The pathways are autophago-lysosome pathway and ubiquitin-proteasome pathway.

Through autophago-lysosome pathway not only protein aggregates but also for instance damaged cell organelles are degraded. There are three primary types of autophagy recognised in mammalian cells thus far: microautophagy, chaperon-mediated autophagy, and macroautophagy. Microautophagy is a non-specific type of autophagy which occurs directly in lysosomes (Marzella et al. 1981). Chaperone-mediated autophagy, on the other hand, is highly specific as chaperones first identify a pentapeptide motif in target proteins (Dice 1990) after which the target protein is degraded in lysosomes (Orenstein & Cuervo 2010). Macroautophagy, like microautophagy, is a non-specific pathway in which autophagosome expands around target molecules and fuses with a lysosome to enable degradation (Yang & Klionsky 2009).

The second pathway for proteolysis of protein aggregates is ubiquitin-proteasome pathway which consists of two distinct yet fully coordinated steps: the covalent attachment of multiple ubiquitin molecules and the degradation by 26S proteasome. The covalent attachment of ubiquitin molecules is carried out by three enzymes, E1, E2, and E3, which all play a unique role in formation and attachment of a polyubiquitin chain (Marx 2002). The degradation by 26S

proteasome begins with a cleavage of the polyubiquitin chain by 19S regulatory particle of 26S and continues with actual degradation by 20S core particle of 26S (Voges et al. 1999). Both, the autophago-lysosome pathway and ubiquitin-proteasome pathway, function in parallel and are thus complementary to each other.

1.2 Skeletal muscle and sarcomere structures

Up to 40% of human body mass consists of skeletal muscle tissue. The skeletal muscles not only enable the movement of our bodies but are also responsible of, for instance, energy metabolism as well as macromolecule turnover and storage. The normal function of skeletal muscles can be affected, for instance, by acute trauma or inherited diseases, such as MFMs. Mature muscle cells do not generally divide but when affected by small acute trauma muscle stem cells called satellite cells can differentiate into mature muscle cells to cure the trauma.

Skeletal muscles are attached to bones by tendons (Figure 1). Each skeletal muscle is surrounded by a membrane called epimysium and consists of a bundle of fascicles (Jorgenson et al. 2020). Each fascicle is, in turn, surrounded by a membrane called perimysium. Inside the perimysium the intermediate space is called endomysium, and within the endomysium are interstitial cells and myofibers. Myofibers are surrounded by sarcolemma and consist of myofibrils and excessive number of mitochondria as muscle cells consume much energy. The striated look of myofibers is caused by thick myosin and thin actin fibres. The muscle cell nuclei, myonuclei, are situated inside the myofibrils and satellite cells outside them. Each myofibril is surrounded by network-like smooth sarcoplasmic reticulum and consists of 2—2.5 μm long sarcomeres which are the smallest functional units of a muscle cell. The bundle structure of a muscle enables the regulation of the whole muscle's contraction as the nerve impulse distributes quickly to the whole myofibril along the sarcolemma. By regulating the amount of contracting myofibers, the precision and strength of each muscle is altered.

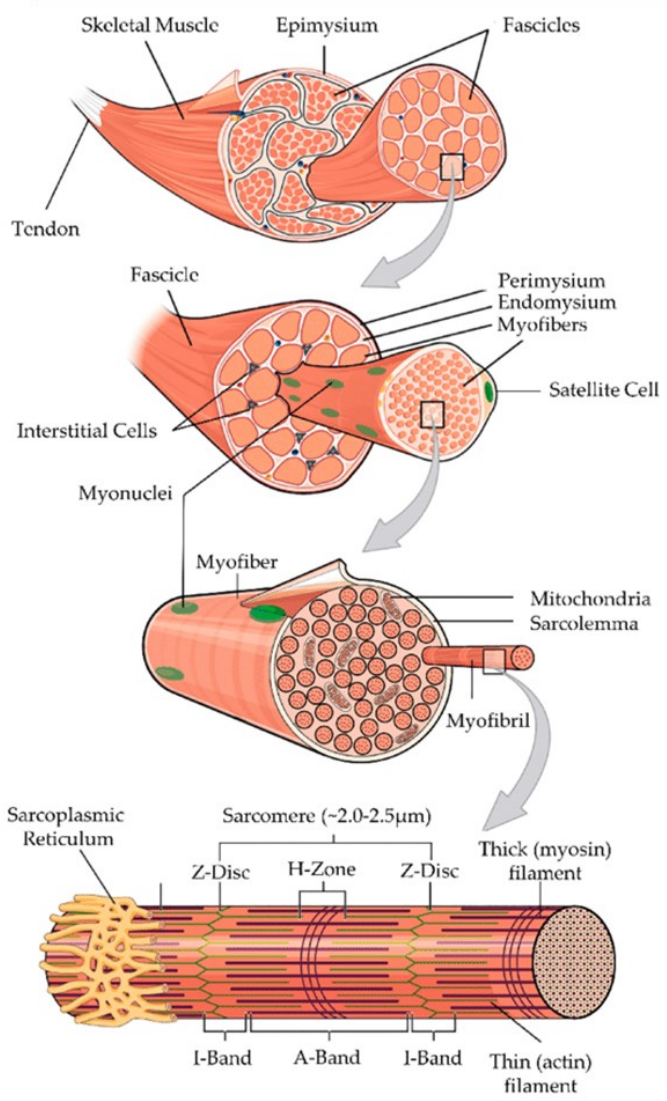

Figure 1. Skeletal muscle structure. A skeletal muscle is built from bundles of muscle cells called myofibers. Myofibers, in turn, consist of a bundle of myofibrils which are built from the smallest functional units of a muscle cell called sarcomeres. The bundle structure of a muscle enables the regulation of contraction as a myofibril always contracts completely (Jorgenson et al. 2020, copyright Jorgenson, Phillips & Hornberger, CC BY 4.0).

MFMs cause disorganisation to the Z-discs of sarcomeres. As the sarcomere structure is biased, the myofibril cannot contract normally and that results as muscle weakness. In sarcomere structure, the Z-disc covers the area where thin actin filaments connect together like a backbone. Multiple different proteins have a crucial role in building this backbone-like structure. For instance, myotilin crosslinks and stabilizes thin actin filaments (Salmikangas et al. 1999), desmin surrounds the sarcomere structure thus stabilizing it (Paulin & Li 2004), and filamin C crosslinks thin actin filaments as well as is in close contact with other surrounding proteins (van der Flier & Sonnenberg 2001). In addition to the Z-disc, the sarcomere structure consists of multiple other areas, such as I-band, H-zone, and A-band (Figure 1) (Jorgenson et al. 2020). I-band covers the area around

Z-disc between the myosin filament heads. H-zone covers the area around myosin backbone where actin filament heads do not reach. And finally, A-band covers the area from one myosin filament head through the myosin backbone to the other head of myosin filament.

1.3 Filamin C functions and structure

Filamin C is a large actin-binding protein. A human genome encodes three filamins: filamin A, filamin B, and filamin C. Whereas filamin C is most abundant in muscle sarcomere structure, filamins A and B are ubiquitously expressed in many cell types and loss-of-function mutations cause defects in brain, vasculature, and bone development (Zhou et al. 2010). Even though these types of filamin function somewhat differently, they all have five generally similar functions: anchoring cortical actin and actin stress fibres to transmembrane receptors, crosslinking actin filaments, bundling parallel actin fibres, and acting as a scaffold to signalling complexes (van der Flier & Sonnenberg 2001). Along with all the actin crosslinking properties, the first mentioned function enables filamin to carry a significant role in cell signalling.

Filamin C localizes not only to Z-discs in muscle sarcomere structure but also to myotendinous junctions, sarcolemma, and intercalated discs (Thompson et al. 2000, van der Ven et al. 2000a, van der Ven et al. 2000b). Purified human filamin C is not yet available and thus the biochemical and biophysical properties of full-length human filamin C have not yet been studied. However, the sequence homology between all three filamin types is > 70% (Kesner et al. 2010) and thus the full-length human filamin C structure and functions can be estimated. The human filamins construct of an N-terminal actin-binding domain (ABD), 24 immunoglobulin (Ig)-like domains, and two calpain hinges between Ig-like domains 15 and 16 (hinge 1) as well as domains 23 and 24 (hinge 2) (Figure 2). In filamins B and C, hinge 1 is spliced out during myogenesis (Thompson et al. 2000, van der Flier et al. 2002) and thus does not exist in mature myofibril protein composition. The Ig-like domains 16—21 contribute to mechanical forces sensing mechanosensory region of filamin C. In muscles, mechanical cues sensing proteins affect cell proliferation and differentiation (Majkut et al. 2014).

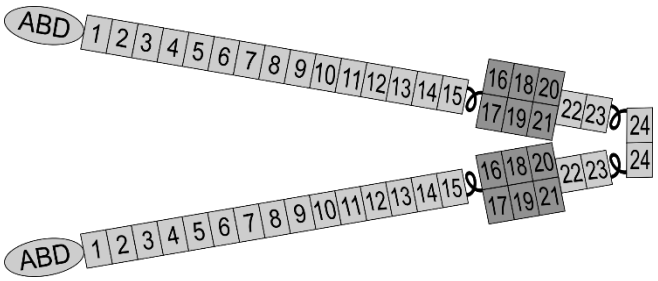

Figure 2. Structure of human filamin C. Filamin C constructs of an ABD, 24 Ig-like domains, and two hinges between domains 15—16 and 23—24. The Ig-like domains 16—21 belong to mechanosensory region and domain 24 to

dimerization site (modified from Huelsmann et al. 2016, copyright Huelsmann et al. 2016, CC BY 4.0).

1.3.1 *Drosophila melanogaster* is used to study filamin C ortholog cheerio

To investigate filamin C functions *in vivo*, *Drosophila melanogaster* is an excellent model organism to use. On a tissue level, the main difference between human and *D. melanogaster* muscle tissue is that *D. melanogaster* expresses only one type of muscle fibre whereas both slow and fast muscle fibres are expressed in human muscles (Poovathumkadavil & Jagla 2020). On a molecular level, the myofibril sarcomere structure of *D. melanogaster* is very similar to the one of human (Hooper & Thuma 2005) as most of human Z-disc proteins have an ortholog in *D. melanogaster* Z-disc structure. The filamin C ortholog in *D. melanogaster* is a protein called cheerio. Cheerio is encoded by a gene called *cher*, and it shares 45% amino acid identity with human filamin C (Ader et al. 2022). Functionally cheerio and human filamin C have similar properties but structurally the main difference is that cheerio has only 22 Ig-like domains instead of the 24 found from human filamin C. The mechanosensing region of cheerio is situated to Ig-like domains 14—19 (Figure 3).

Investigating the protein functions in model organisms enables one to modify the primary, secondary, tertiary, or even quaternary structures of the protein of interest. One can, for instance, mutate the amino acid sequence of the protein to alter the secondary structure and thus the functionality of the protein. The addition of specific markers, such as green fluorescent protein (GFP) tag, is also possible and allows one to visualize the protein in downstream experiments. For instance, Huelsmann et al. (2016) investigated how the functions of cheerio would change when mutations were created to Ig-like domains 16 and 18 on the mechanosensory region.

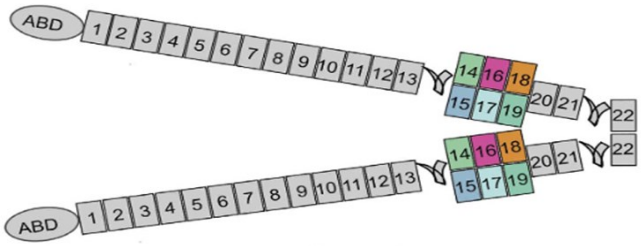

Figure 3. Structure of cheerio. Cheerio constructs of an ABD, 22 Ig-like domains, and two hinges between domains 13—14 and 21—22. The Ig-like domains 14—19 belong to mechanosensory region and domain 22 to dimerization site (Huelsmann et al. 2016, copyright Huelsmann et al. 2016, CC BY 4.0).

1.4 Aims of the study

Myofibrillar myopathies (MFMs) are defined by myofibrillar degradation and especially accumulation of the degradation products (Nakano et al. 1996). In filaminopathy, which is a type of MFM, the accumulation is related specifically

to filamin protein. The aim of this study was to investigate protein aggregation in filaminopathy with filamin C ortholog cheerio in *D. melanogaster* fruit fly. It is previously known that when mutated to be open from two sites at the mechanosensor region, cheerio is eager to form aggregates (Green et al. 2018). What is yet to be understood is if the open mutation only occurred at one site of the mechanosensor region, would aggregates still be formed and if so, would the formed aggregates still be similar to double-open aggregates in size and shape. Based on this, my research questions are as follows:

1. Does single-open mutation cause similar number of aggregates as double-open mutation and if so, would the aggregates be similar in volume?
2. Does the number and volume of single-open aggregates increase upon time?
3. Does the shape differ between single-open aggregates and double-open aggregates, and does the shape of single-open aggregates change upon time?

In principle, protein folding is based on hiding hydrophobic regions of amino acid chain inside the secondary structures of a protein. Protein aggregation is caused when these hydrophobic regions are exposed to the surrounding environments. When cheerio is mutated to be open from one site (single-open) at domain 16, hydrophobic side chain owning isoleucine (Ile) is replaced with negatively charged side chain owning glutamic acid (Glu). This changes the charge and hydrophobicity of the amino acid chain and thus alters the secondary structure when the amino acid chain folds. Hence, I hypothesize that single-open mutation in cheerio would cause aggregation. However, as the mutation only occurs at one domain, I hypothesize that the formed aggregates would be smaller in volume than when the mutation occurs at two domains (double-open) as less hydrophobic regions are exposed.

MFMs are known to be progressive diseases with muscle weakness as the most abundant symptom. The muscle weakness is caused by the accumulation of degradation products into protein aggregates and thus disorganization of Z-discs. Due to the progressive nature of MFMs, I hypothesize that the number and volume of aggregates increases upon time. If the volume of the aggregates increases that must affect the shape of the aggregates as well. The double-open mutation in cheerio is known to cause hammerhead-like shaped aggregates (Green et al. 2018) which can thus be classified as particulates rather than, for example, fibrils or gels by shape. As the volume of a particulate aggregate increases, the shape of the aggregate does not necessarily elongate as in fibril aggregate, but rather expands in any direction. Based on this, I hypothesize that the single-open aggregates are similar in shape with the double-open aggregates. Also, due to growth in volume, I hypothesize that the single-open cheerio aggregates expand evenly to every direction and thus the shape of the aggregates does not necessarily change.

2 MATERIALS AND METHODS

2.1 Materials

Three different fly lines were used in the experiment (Table 1). All of them contained monomeric green fluorescent (mGFP) protein inserted in-frame in the genomic sequence of fly filamin cheerio. The wild-type (WT) and double-open mutations were described in Huelsmann et al. 2016 and the single open mutation was generated by Hannah Green with the same method (Hannah Green and Jari Ylänne, unpublished). Flies from each genotype were kept in cultivation vials that contained Nutri-Fly Bloomington Formulation (Genesee Scientific). The fly vials were maintained at +22 ˚C and the circadian rhythm was controlled with 12h light and 12 h dark cycle.

Table 1. Fly line genotypes.

Fly line	Genotype
WT	w;;P{ry[+t7.2]=neoFRT}82B GT{cher[GFP_mGFP6-2]}
single-open	w;;P{ry[+t7.2]=neoFRT}82B GT{ cher[single-open MSR][GFP_mGFP6-2]}
double-open	w;;P{ry[+t7.2]=neoFRT}82B GT{cher[open MSR][GFP_mGFP6-2]}

In the single-open mutation of cheerio, Ile was substituted with Glu in the Ig-like domain 16 to generate negative charge to the primary structure (Figure 4). This prevents the correct folding on the secondary structure generating an open mutation to the conformation of cheerio. In the double-open mutation, a similar mutation was expressed also in the Ig-like domain 18.

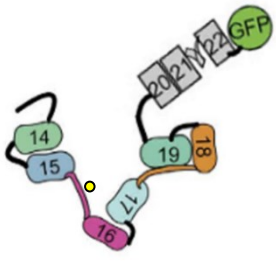

Figure 4. Single-open mutated cheerio. The single-open mutation was expressed on Ig-like domain 16 in which isoleucine (Ile) was replaced with glutamic acid (Glu) (yellow dot). A monomeric green fluorescent protein (mGFP) tag was fused at the dimerization domain (22) to visualize cheerio under confocal microscope (modified from Huelsmann et al. 2016, copyright Huelsmann et al. 2016, CC BY 4.0).

I imaged indirect flight muscles from x individual WT and y single-open mutant flies 0—6 h, 24 h, and 14 d after hatching. In addition, I used for analysis images taken by Dr. Katariina Kiviaho from 10 double-open and 10 WT flies 24 h after hatching. The images by Dr. Kiviaho had only the phalloidin channel.

2.2 Methods

2.2.1 Mutation site sequencing of fly lines

The correct mutation sites were ensured by sequencing the domain regions 16—18 of WT and single-open fly lines. Genomic DNA from three homozygous males of each fly line was extracted via mechanically smashing the flies with smashing buffer (10 mM Tris pH 8.0, 25 mM NaCl, 1 mM EDTA) including 1:100 20 mg/ml proteinase K. The fly smash was incubated at +55 ˚C for 45 min after which the proteinase K was inactivated at +95 ˚C for 10 min. The supernatant of the fly smash was stored in -20 ˚C for further use.

PCR was performed with genomic fly DNA samples as well as positive and negative controls. Each PCR reaction contained 5 ng template DNA, 200 µM each dNTP (ThemoScientific), 0.5 µM each primer (Table 2), 1X Phusion Green HF buffer (ThermoScientific), and DNA polymerase (Phusion PLUS, ThemoScientific). Thermal cycling conditions were 30 s +98 ˚C, followed by 27 cycles of 20 s +98 ˚C, 20 s +60 ˚C, and 20 s +72 ˚C, and a final extension of 5 min at +72 ˚C. PCR products were purified and sequenced by Macrogen (Amsterdam, Netherlands) using primers presented in Table 3.

TABLE 2. PCR primer nucleotide sequences.

	Nucleotide sequence
forward	TATGTGACTGCCTACGGACCCGGCCTG
reverse	CGCATCCGGGGAGACGTACACCTTG

TABLE 3. Sequencing primer nucleotide sequences.

	Nucleotide sequence
forward	TCCTTGCCAGGACACAAACATT
forward	CGGAACTGGCCTCAAGGAGGGT
reverse	ACGCTTCACCGACACCAGATGC
reverse	TCTCCGCATCCTCGGTCACGTT
reverse	AATTGGTAGGGAGCGTCCGCCT

Sequence analysis was performed with Benchling's sequence tool (Biology software, 2023, retrieved from https://benchling.com). Acquired sequences were trimmed to good quality and aligned with MAFFT against cher mRNA transcript (FlyBase ID: FBtr0479929).

2.2.2 Confocal imaging of indirect flight muscles

Prior to imaging, the indirect flight muscles of male flies at timepoints 0—6 h, 24 h, and 14 d were dissected in relaxing solution (20 mM sodium phosphate buffer, 5 mM $MgCl_2$, 5 mM EGTA, 5 mM adenosine trisphosphate, 0.3% Triton-X), fixed with 4% paraformaldehyde in phosphate buffered saline and stained with 1:200 phalloidin (Alexa Fluor 555, ThermoScientific) in 0.5% bovine serum albumin in phosphate buffered saline at +4 ˚C overnight. After removal of the staining solution and washing three times with 0.3% Triton-X in phosphate buffered saline for 15 min, the indirect flight muscles were dissected and mounted in Vectashield (Vector Laboratories). Samples were imaged with a 60x oil objective (N.A. 1.4, WD 0.13) on A1R (Nikon, 2013) confocal microscope. 488 nm Argon laser excitation and 515/30 nm emission filter was used for GFP, and 561 nm Sapphire laser excitation and 595/50 nm emission filter was used for phalloidin. Three 10 µm stack images were acquired from each individual with 0.33 µm interval on z-axis using 0.10 µm pixel size and 1024x1024 scan size.

2.2.3 Image analysis and statistical testing

For the image analysis, only the channel detecting phalloidin was used as the obtained external data set did not include the channel detecting GFP. A macro was written for ImageJ2 Fiji (version 1.54f) and used for detection of cheerio aggregates as regions of interest (ROIs) (Appendix 1). The ROI detection was based on thresholded images. ROIs on the edges of the stack images were excluded. The volume for cheerio aggregates in detected ROIs was calculated in μm^3 from ROIs. If a ROI included more than one cheerio aggregate, volume would not be calculated. The rest of the analysis was conducted from Z-projections of the ROIs.

The ROI detection data was blindly validated by checking if each detected ROI actually included one or more cheerio aggregates. All data was then filtered so that the falsely detected ROIs and thus their volumes were excluded from further analysis. The number of aggregates was calculated from the number of detected and validated ROIs so that each ROI was considered as one aggregate.

The shape of the cheerio aggregates was determined with an attribute roundness in ImageJ. Roundness differentiates between robust and smooth surface of a particle and can thus detect differences between unevenly (values closer to 0.00) and evenly shaped (values closer to 1.00) cheerio aggregates. The roundness was measured from thresholded ROI stack images acquired from the detection of ROIs in the aggregate volume measurement (Appendix 2). ImageJ calculates the roundness based on the ratio of the area and major axis of the detected particle (Equation 1) from a Z-projection.

$$Roundness = 4 \times \frac{[Area]}{\pi \times [Major\ axis]^2} \quad (1)$$

All data filtering, plotting, and statistical testing was performed in R Studio (version 2023.12.1). Homogeneity of variance between groups of each data set was tested with Levene's test and data normality with Shapiro-Wilk's test. Based on whether the data set was or was not homogenic or normal, a suitable test for determination of significance was chosen accordingly: Welch's t-test for the number of cheerio aggregates at 24 h and roundness of cheerio aggregates at 24 h, Mann-Whitney U-test for the volume of cheerio aggregates at 24 h, ANOVA for the number of cheerio aggregates upon time, Kruskal-Wallis for the volume of cheerio aggregates upon time and Dunn's test for pairwise testing, and one-way ANOVA for roundness of cheerio aggregates upon time and Tuckey's honestly significant difference test for pairwise testing. Significance level was determined to $p < 0.05$ in all tests.

3 RESULTS

3.1 Single-open mutation was expressed homozygously

The correct mutations sites of WT and single-open fly lines were ensured by sequencing. For single-open, Ile to Glu mutation was detected in Ig-like domain 16 (Table 3). In Ig-like domain 18, WT sequence was detected to cause the open conformation mutation only in Ig-like domain 16. The mutation at Ig-like domain 16 was homozygous. For WT genotype, no mutations were detected in either Ig-like domains 16 and 18.

TABLE 3. Nucleotide sequences around open conformation mutation sites in Ig-like domains 16 and 18. The mutation site codon is bolded. The mutation sites for three sequenced individuals from each fly line are shown. The mutation site sequences present homozygosity across all individuals. Cher mRNA transcript (FlyBase ID: FBtr0479929) was used as a reference.

Fly line	Nucleotide sequence	
	Ig-like domain 16	Ig-like domain 18
Reference	CGC AAC CAG **ATC**[1] TCG	CGC GAG AAG **ATC** CAG
Single-open	CGC AAC CAG **GAG**[2] TCG	CGC GAG AAG **ATC** CAG
	CGC AAC CAG **GAG** TCG	CGC GAG AAG **ATC** CAG
	CGC AAC CAG **GAG** TCG	CGC GAG AAG **ATC** CAG
WT	CGC AAC CAG **ATC** TCG	CGC GAG AAG **ATC** CAG
	CGC AAC CAG **ATC** TCG	CGC GAG AAG **ATC** CAG
	CGC AAC CAG **ATC** TCG	CGC GAG AAG **ATC** CAG

[1] ATC is a codon for ILE.
[2] GAG is a codon for GLU.

3.2 Single-open aggregates are fewer but larger than double-open aggregates

The number and volume of aggregates produced from the WT, single-open, and double-open genotypes was compared at 24 h after hatching. The average number of aggregates with single-open and double-open mutations were 16.2±2.5 and 32.2±6.9, respectively. The mean represents the average number of aggregates observed within each genotype, while the standard error indicates the variability of the mean estimate. The single-open genotype produced less aggregates than double-open genotype ($p = 0.053$, Welch's t-test) (Figure 5A-C). However, the single-open aggregates appeared larger in volume than double-open aggregates ($p < 0.05$, Mann-Whitney U-test) (Figure 5D). The average volume of aggregates with single-open and double-open mutations were 18.3±1.1 µm^3 and 8.7±0.5 µm^3, respectively. The WT genotype was excluded from analysis due to small number of individuals (n = 3) from which ROIs were detected.

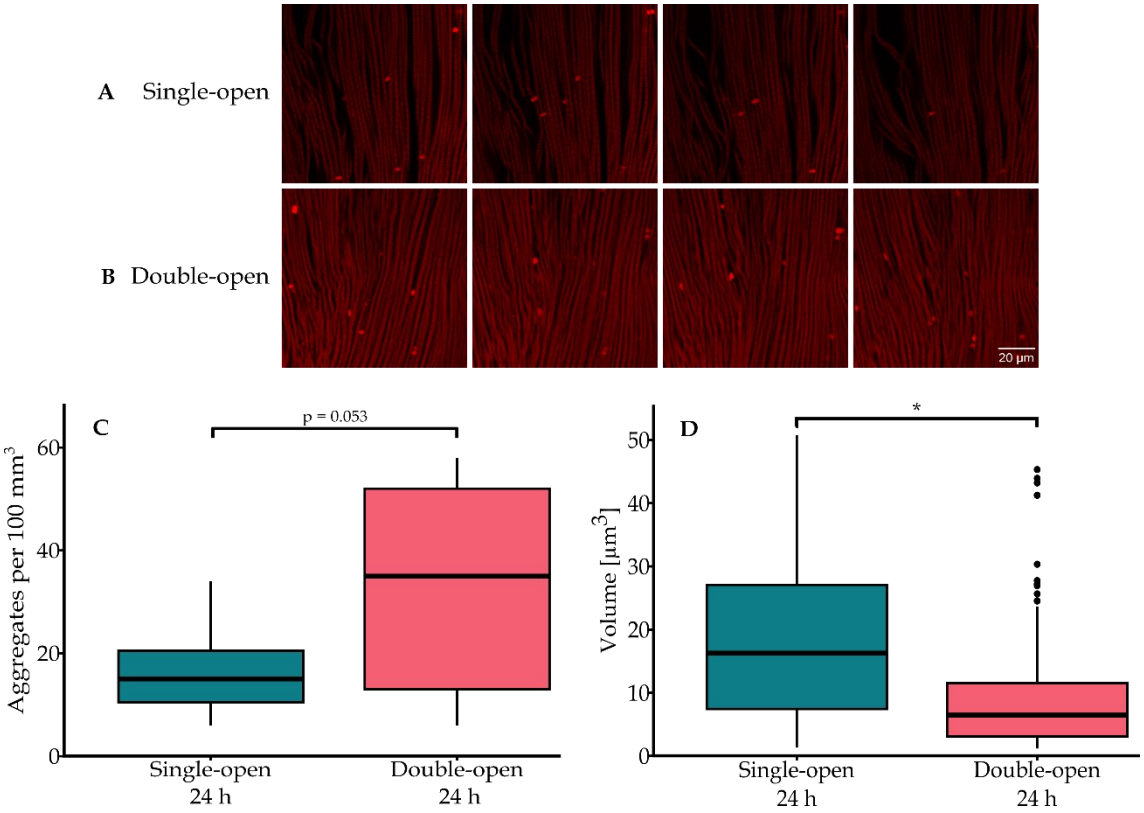

Figure 5. Cheerio aggregate number and volume with single-open and double-open mutations. Four confocal sections with 2.3 µm z-intervals from A) single-open and B) double-open flight muscles. C) Quantitation of the number of actin-containing protein aggregates in single-open individuals (n = 11) and double-open individuals (n = 9). Note that single-open flies contained significantly less aggregates. D) The volume [µm^3] of the cheerio single-open aggregates (n = 128) was larger than the double-open aggregates (n = 245). Horizontal middle lines of boxes indicate the median value, boxes contain the middle 50% of data, and

whiskers indicate variability outside the upper and lower quartiles of data. Outliers are indicated as dots. * $p < 0.05$.

3.3 Volume of single-open aggregates increases upon time

The change in the cheerio single-open aggregate number and volume was measured upon time. The chosen timepoints were right after hatching (0—6 h), at full maturation (24 h), and aged individuals (14 d) as *D. melanogaster* typical lifespan is around four weeks. No significant change was observed in the aggregate number ($p = 0.674$, one-way ANOVA) (Figure 6A). The volume of the aggregates, on the other hand, increased upon time ($p < 0.05$, Kruskal-Wallis) (Figure 6B, Figure 7D-F).

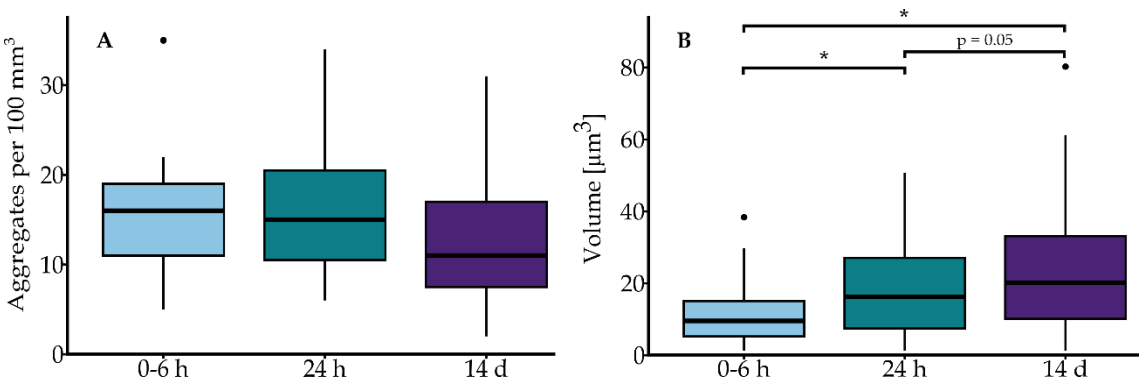

Figure 6. Change in cheerio single-open aggregate number and volume upon time. A) No significant change was observed in the aggregate number of cheerio with single-open mutation ($p = 0.674$, one-way ANOVA). The sample sizes were n = 9 (0—6 h), n = 11 (24 h), and n = 11 (14 d). Aggregate number is expressed in 100 mm^3 of muscle tissue. B) The aggregate volume [μm^3] upon time was measured at same timepoints (0—6 h: n = 76, 24 h: n = 128, and 14 d: n = 76). Significant change in volume was observed between timepoints 0—6 h and 24 h as well as 0—6 h and 14 d. See Figure 5 for detailed information on figure legends.

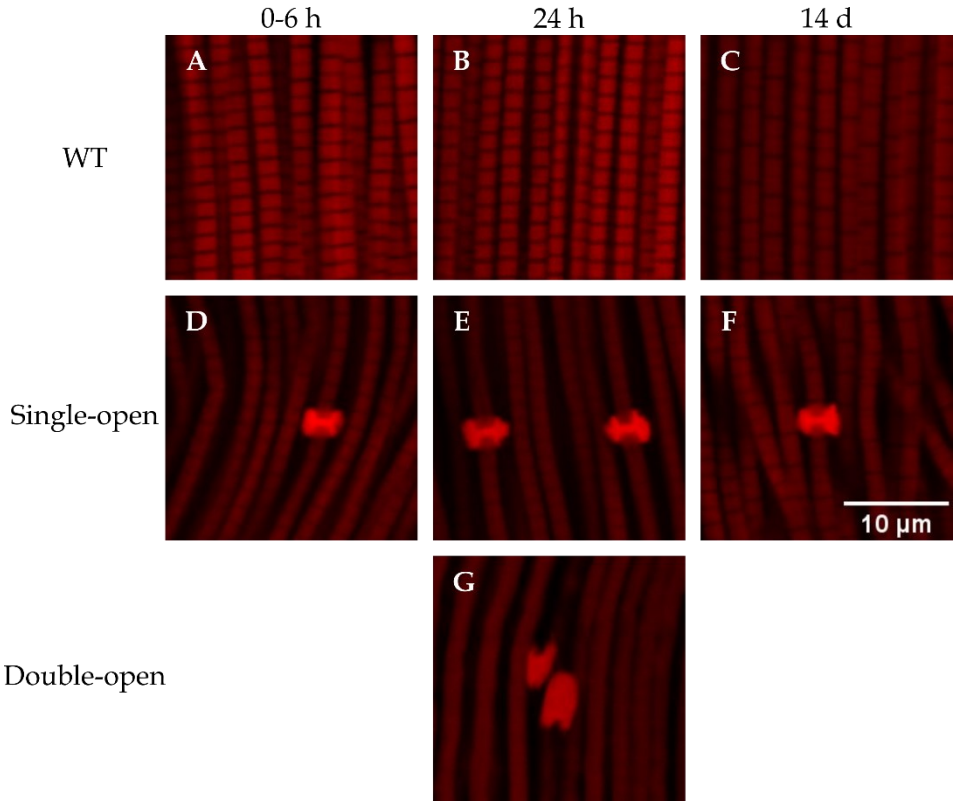

Figure 7. Cheerio aggregates expressed by different genotypes. (A-C) WT did not express any aggregates at any timepoint. (D-F) The volume of hammerhead-like shaped single-open aggregates grew upon time. Single-open aggregates were situated precisely on Z-discs. (G) Double-open aggregates were found from between myofibrils.

3.4 The shape of cheerio aggregates differs between genotypes and changes upon time

The shape of the cheerio aggregates varied between the single-open and double-open aggregates. The single-open aggregates were hammerhead-like by shape whereas double-open aggregates were oval by shape (Figure 7D-G). The single-open aggregates also stayed within the Z-disc structures whereas double-open aggregates were situated in between the sarcomeres.

The difference between the shape of the single-open and double-open aggregates was also detected statistically with an ImageJ attribute roundness. At 24 h after hatching, the single-open aggregates showed less round shape than double-open aggregates ($p < 0.05$, Welch's t-test) (Figure 8A). Interestingly, the double-open aggregates showed separation into two different populations of roundness: one less round and other rounder. The less round double-open aggregates were often arrow-head shape (Figure 7G).

The change of the single-open aggregate shape was measured statistically with the same attribute roundness. At timepoints 0—6 h, 24 h, and 14 d after

hatching, the roundness of the aggregates shifted from less round to rounder, respectively ($p < 0.05$, one-way ANOVA) (Figure 8B). The average roundness of single-open aggregates at the chosen timepoints were 0.614±0.01, 0.596±0.01 and 0.683±0.01, respectively. At 24 h after hatching, a so-called intermediate state can be observed where there are both less round and rounder shaped aggregates.

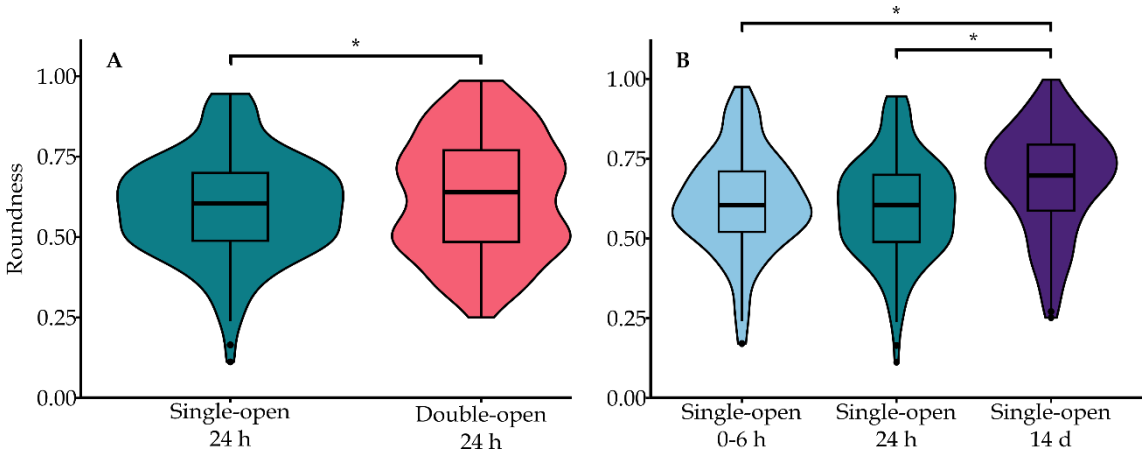

Figure 8. Shape of the cheerio aggregates. A) At 24 h after hatching, cheerio single-open aggregates show less round shape than cheerio double-open aggregates ($p < 0.05$, Welch's t-test). From double-open aggregates two populations can be observed: one with less round and other with rounder shape. B) Upon time, single-open aggregates showed a change from less round to rounder in shape ($p < 0.05$, one-way ANOVA). The sample sizes for the timepoints were n = 146 (0—6 h), n = 177 (24 h), and n = 146 (14 d). See Figure 5 for detailed information on figure legends.

4 DISCUSSION

In this study, the aggregation of *Drosophila melanogaster* filamin, cheerio, was studied by an open conformation mutation (single-open) in the mechanosensory region. A two-site open conformation mutation (double-open) in cheerio is known to cause aggregation (Green et al. 2018). I found that the single-open mutation causes aggregation. Although the number of single-open aggregates was lower than the number of aggregates caused by the double-open mutation, single-open aggregates were larger in volume than double-open aggregates. The volume shape of the single-open aggregates changed upon aging.

No significant change in the number of single-open aggregates upon aging was observed. This suggests that the early stages of single-open aggregates are formed during myogenesis, the development of muscle cells. Myogenesis does generally not occur in large quantities after the development of muscle tissues. Filamin is, however, known to play a significant role in the early developmental stages of *D. melanogaster* (Huelsmann et al. 2016). It thus seems that either new aggregates are not formed during the adult life of an individual or the number of

new aggregates does not exceed the aggregate clearance mechanisms' ability to degrade aggregates.

The function of protein clearance mechanisms is affected negatively by aging as the cells' ability to degrade misfolded proteins is decreased (Saez & Vilchez 2014). This leads to accumulation of misfolded proteins. Due to accumulation, the misfolded proteins interact with already existing protein aggregates thus increasing their volume. Several filamin binding proteins, such as actin, have been shown to be involved in the protein aggregates of filaminopathy (Kley et al. 2013). Indeed, the involvement of actin in protein aggregates was observed (Figure 7). It is likely that mutations in filamin only serve as a platform for aggregate formation. As the aggregate then develops, other associating proteins become involved as well.

Single-open aggregates are formed directly at the Z-disc structures of a sarcomere (Figure 7D-F). The double-open aggregates, in turn, are located in between myofibrils (Figure 7G). The difference in location could explain why there are less single-open than double-open aggregates as the aggregate clearance mechanisms might react differently to aggregates located inside rather than outside myofibrils. To investigate this, the protein composition of single- and double-open aggregates could be determined as it could enlighten the differently located aggregates' interactions with aggregate clearance mechanisms. This is because proteins of the clearance mechanisms are known to be involved in muscle protein aggregates (Ayyadevara et al. 2016). Furthermore, it would be interesting to analyse the double-open aggregates at earlier timepoints. Are they then located at Z-disc like the single-open aggregates? Due to limitations of time, this could not be done during this study.

The single- and double-open aggregates' differing locations could also explain why they are shaped differently. On one hand, single-open aggregates were found to be shaped like hammerheads (Figure 7D-F). The localization to the Z-disc seems to limit the shape of single-open aggregates leading to the aggregates to burst out of the Z-discs creating the hammer ends. Double-open aggregates, on the other hand, are not limited by the Z-disc structure as they are located in between myofibrils. This enables their shape to grow oval. Interestingly, double-open aggregates express two populations of roundness (Figure 8A). This could be explained by the ovality of the aggregates not being symmetrical. In such case, the orientation of the aggregate distorts the interpretation of the shape in the image. To get a better understanding of the shapes of the aggregates, other shape attributes, such as circularity or axis ratio, should be measured as well. Also, other imaging methods, such as electron microscopy, could provide more accurate understanding of the aggregates' shape.

An important observation was also that single-open aggregates seem to have an increase in volume simultaneously with the shape growing rounder upon time (Figure 6B, 8B). As the volume of a single-open aggregate increases, its hammer ends seem to grow (Figure 7D, F). This leads to rounder appearance

of the aggregates. To ensure the correlation between the changes in volume and roundness upon time, statistical testing should be conducted.

While this thesis contributes valuable insights into fine tuning muscle protein aggregates, it is essential to acknowledge certain limitations inherent in this study. This study was conducted with all male panel of *D. melanogaster*. When interpreting the results, it must therefore be remembered that differences between the sexes have not been considered. Furthermore, although human and *D. melanogaster* muscle tissues are very similar in structure, the structure is simplified in *D. melanogaster*. What comes to the measurements made from the confocal image data, firstly, the detection of filamin aggregates images relied on a channel detecting phalloidin staining of the sample. Utilizing the detection of mGFP tag of filamin could have given more precise data for aggregate number, volume, and shape measurements. However, this was not possible in this thesis as the external data set did not include the GFP detecting channel. The measurements of the number, volume, and shape of aggregates were also significantly affected by thresholding and the use of Z-projection in image processing. These image processing tools weaken the particles' precise niches of shape which results in more averaged measurement results.

Altogether, the findings of this thesis are in line with the known effects of protein aggregates causing filaminopathy. The most essential symptom of filaminopathy is progressive muscle weakness. Pathologically, muscle weakness results from the disintegration of the Z-disc structure caused by protein aggregates (Nakano et al. 1996, Selcen 2011). Based on the findings of this thesis, I suspect that the progressiveness of muscle weakness is caused by increase in aggregate volume rather than increase in aggregate number as first hypothesized. In addition, the progressiveness could be a result of instability of normal protein turnover as the clearance mechanisms of misfolded proteins is weakened in aging cells.

Protein aggregates are the main pathological cause not only in myofibrillar myopathies but also in other diseases such as Alzheimer's and Parkinson's disease (Irvine et al. 2008). As a result of research on, for example, these diseases, the interactions of protein aggregates to their surroundings as well as the protein composition of aggregates have already been studied to some extent (e.g., Ayyadervara et al. 2016, Green et al. 2018). However, other properties of protein aggregates, such as shape and location, have not been under further interest thus far. Greater understanding on the properties of protein aggregates, how and when aggregates are formed, and the effects of differing mutations would be relevant in developing new treatment strategies for filaminopathy.

5 CONCLUSIONS

The results of this thesis confirm that firstly, only one domain pair open conformation mutation in filamin mechanosensory region is sufficient for serving as a seed for protein aggregate formation. Secondly, aging seems to impair the ability of muscle cells to deal with misfolded proteins which results in increasement of protein aggregate's volume. And thirdly, the increasement in volume together with the location of the aggregates seem to affect the shape of the protein aggregates. A more comprehensive understanding of muscle protein aggregate characteristics is a prerequisite to developing new treatment strategies for muscle weakness diseases.

ACKNOWLEDGEMENTS

This Pro Gradu was carried out at University of Jyväskylä, Department of Biological and Environmental Science and Nanoscience centre, and funded by the Research Council of Finland grant 343444 to Professor Jari Ylänne. I would like to thank my supervisors Professor Jari Ylänne and MSc Riku Korkiamäki not only for this fascinating topic but also for patient guidance throughout this project. Also, I would like to thank Dr. Katariina Kiviaho for introducing me to the laboratory work with flies as well as to the capricious soul of Nikon A1R microscope.

Jyväskylä May 2, 2024
Kerttu Kotala

REFERENCES

Ader F., Russi M., Tixier-Cardoso L., Jullian E., Martin E., Richard P., Villard E. & Monnier V. 2022. Drosophila CRISPR/Cas9 mutants as tools to analyse cardiac filamin function and pathogenicity of human FLNC variants. *Biol. Open* 11: bio059376, doi: 10.1242/bio.059376.

Ayyadevara S., Balasubramaniam M., Suri P., Mackintosh S.G., Tackett A.J., Sullivan D.H., Shmookler Reis R.J. & Dennis R.A. 2016. Proteins that accumulate with age in human skeletal-muscle aggregates contribute to declines in muscle mass and function in Caenorhabditis elegans. *Aging* 8: 3486–3496, doi: 10.18632/aging.101141.

Dalkilic I., Schienda J., Thompson T.G. & Kunkel L.M. 2006. Loss of FilaminC (FLNc) results in severe defects in myogenesis and myotube structure. *Mol. Cell Biol.* 26: 6522–6534, doi: 10.1128/MCB.00243-06.

Dice J.F. 1990. Peptide sequences that target cytosolic proteins for lysosomal proteolysis. *Trends Biochem. Sci.* 15: 305—309, doi: 10.1016/0968-0004(90)90019-8.

Fürst D.O., Goldfarb L.G., Kley R.A., Vorgerd M., Olivé M. & Ven P.F.M. van der. 2013. Filamin C-related myopathies: pathology and mechanisms. *Acta neuropathol.* 125: 33–46, doi: 10.1007/s00401-012-1054-9.

Giurleo J.T., He X. & Talaga D.S. 2008. Beta-lactoglobulin assembles into amyloid through sequential aggregated intermediates. *J. Mol. Biol.* 381: 1332—1348, doi: 10.1016/j.jmb.2008.06.043.

Green H.J., Griffiths A.G., Ylänne J. & Brown N.H. 2018. Novel functions for integrin-associated proteins revealed by analysis of myofibril attachment in Drosophila. *eLife* 7: e35783, doi: 10.7554/eLife.35783.

Hooper S.L. & Thuma J.B. 2005. Invertebrate muscles: muscle specific genes and proteins. *Physiol. Rev.* 85: 1001–1060, doi: 10.1152/physrev.00019.2004.

Huelsmann S., Rintanen N., Sethi R., Brown N.H. & Ylänne J. 2016. Evidence for the mechanosensor function of filamin in tissue development. *Sci. Rep.* 6: 32798, doi:10.1038/srep3279.

Irvine G.B., El-Agnaf O.M., Shankar G.M. & Walsh D.M. 2008. Protein Aggregation in the Brain: The Molecular Basis for Alzheimer's and Parkinson's Diseases. *Mol. Med.* 14: 451–464, doi: 10.2119/2007-00100.Irvine.

Jorgenson K., Phillips S. & Hornberger T. 2020. Identifying the Structural Adaptations that Drive the Mechanical Load-Induced Growth of Skeletal Muscle: A Scoping Review. *Cells* 9: 1658, doi:10.3390/cells9071658.

Kesner B.A., Milgram S.L., Temple B.R. & Dokholyan N.V. 2010. Isoform divergence of the filamin family of proteins. *Mol. Biol. Evol*. 27: 283–295, doi: doi.org/10.1093/molbev/msp236.

Kley R.A., Maerkens A., Leber Y., Theis V., Schreiner A., Van Der Ven P.F.M., Uszkoreit J., Stephan C., Eulitz S., Euler N., Kirschner J., Müller K., Meyer H.E., Tegenthoff M., Fürst D.O., Vorgerd M., Müller T. & Marcus K. 2013.

A Combined Laser Microdissection and Mass Spectrometry Approach Reveals New Disease Relevant Proteins Accumulating in Aggregates of Filaminopathy Patients. *Molecular & Cellular Proteomics* 12: 215–227, doi: 10.1074/mcp.M112023176.

Majkut S., Dingal P.C.D.P. & Discher D. E. 2014. Stress sensitivity and mechanotransduction during heart development. *Curr. Biol*. 24: R495–R501, doi: 10.1016/j.cub.2014.04.027.

Marx J. 2002. Cell biology. Ubiquitin lives up to its name. *Science* 297: 1792—1794, doi: 10.1126/science.297.5588.1792.

Marzella L., Alhberg J. & Glaumann H. 1981. Autophagy, heterophagy, microautophagy and crinophagy as the means for intracellular degradation. *Virchows. Arch. B Cell Pathol. Incl. Mol. Pathol.* 36: 219—234, doi: 10.1007/BF02912068.

Nakano S., Engel A.G., Waclawik A.J., Emslie-Smith A.M. & Busis N.A. 1996. Myofibrillar myopathy with abnormal foci of desmin positivity. I. Light and electon microscopy analysis of 10 cases. *J. Neuropathol. Exp. Neurol.* 55: 549—562, doi: 10.1097/00005072-199605000-00008.

Olivé M., Kley R.A. & Goldfarb L.G. 2013. Myofibrillar myopathies: new developments. *Curr. Opin. in Neurology* 26: 527–535, doi: 10.1097/WCO.0b013e328364d6b1.

Orenstein S.J. & Cuervo A.M. 2010. Chaperone-mediated autphagy: molecular mechanisms and physiological relevance. *Semin. Cell Dev. Biol.* 21: 719—726, doi: 10.1016/j.semcdb.2010.02.005.

Paulin D. & Li Z. 2004. Desmin: a major intermediate filament protein essential for the structural integrity and function of muscle. *Exp Cell Res*. 301: 1–7, doi:10.1016/j.yexcr.2004.08.004. PMID: 15501438.

Poovathumkadavil P. & Jagla K. 2020. Genetic Control of Muscle Diversification and Homeostasis: Insights from Drosophila. *Cells* 9: 1543, doi: 10.3390/cells9061543.

Saez I. & Vilchez D. 2014. The mechanistic links between proteasome activity, aging, and age-related diseases. *Curr. Genomics* 15: 38—51, doi: 10.2174/138920291501140306113344.

Salmikangas P., Mykkänen O.M., Grönholm M., Heiska L., Kere J., Carpén O. 1999. Myotilin, a novel sarcomeric protein with two Ig-like domains, is encoded by a candidate gene for limb-girdle muscular dystrophy. *Hum. Mol. Genet*. 8:1329-1336, doi:10.1093/hmg/8.7.1329.

Selcen D. 2011. Myofibrillar myopathies. *NMD* 21: 161–171, doi: 10.1016/j.nmd.2010.12.007.

Singh L.R., Dar T.A., Rahman S., Jamal S. & Ahmad F. 2009. Glycine betaine may have opposite effects on protein stability at high and low pH values. *Biochim. Biophys. Acta.* 1794: 929—935, doi: 10.1016/j.bbapap.2009.02.005.

Thompson T.G., Chan Y.M., Hack A.A., Brosius M., Rajala M., Lidov H.G., McNally E.M., Watkins S. & Kunkel L.M. 2000. Filamin 2 (FLN2): A muscle-specific sarcoglycan interacting protein. *J. Cell Biol*. 148: 115–126, doi: 10.1083/jcb.148.1.115.

van der Flier A., Kuikman I., Kramer D., Geerts D., Kreft M., Takafuta T., Shapiro S.S. & Sonnenberg A. 2002. Different splice variants of filamin-B affect myogenesis, subcellular distribution, and determine binding to integrin [beta] subunits. *J. Cell Biol*. 156: 361–376, doi: 10.1083/jcb.200103037.

van der Flier A. & Sonnenberg A. 2001. Structural and functional aspects of filamins. *Biochim. Biophys. Acta* 1538: 99—117, doi: 10.1016/s0167-4889(01)00072-

van der Ven P.F., Obermann W.M., Lemke B., Gautel M., Weber K. & Furst D.O. 2000a. Characterization of muscle filamin isoforms suggests a possible role of gamma-filamin/ABP-L in sarcomeric Z-disc formation. *Cell Motil. Cytoskelet*. 45: 149–162, doi: 10.1002/(SICI)1097-0169(200002)45:2<149::AID-CM6>3.0.CO;2-G.

van der Ven P.F., Wiesner S., Salmikangas P., Auerbach D., Himmel M., Kempa S., Hayess K., Pacholsky D., Taivainen A., Schroder R., Carpén O. & Fürst D.O. 2000b. Indications for a novel muscular dystrophy pathway: gamma-filamin, the muscle-specific filamin isoform, interacts with myotilin. *J. Cell Biol*. 151: 235–248, doi: 10.1083/jcb.151.2.235.

Voges D., Zwickl P. & Baumeister W. 1999. The 26S proteasome: a molecular machine designed for controlled proteolysis. *Annu. Rev. Biochem.* 68: 1015—1068, doi: 10.1146/annurev.biochem.68.1.1015.

Vorgerd M., van der Ven P.F.M., Bruchertseifer V., Löwe T., Kley R.A., Schröder R., Lochmúller H., Himmel M., Koehler K., Fürst D.O. & Huebner A. 2005. A mutation in the dimerization domain of filamin c causes a novel type of autosomal-dominant myofibrillar myopathy. *Am. J. Hum. Genet*. 7: 297–304, doi: 10.1086/431959.

Wang W., Nema S. & Teagarden D. 2010. Protein aggregation—Pathways and influencing factors. *Int. J. Pharm.* 390: 89–99, doi: 10.1016/j.ijpharm.2010.02.025.

Zhou A.-X., Hartwig J.H. & Akyürek L.M. 2010. Filamins in cell signaling, transcription and organ development. *Trends in Cell Biology* 20: 113—123, doi: 10.1016/j.tcb.2009.12.001.

Yang Z. & Klionsky D.J. 2009. On overview of the molecular mechanism of autophagy. *Curr. Top. Microbiol. Immunol*. 335: 1—32, doi: 10.1007/978-3-642-00302-8_1.

APPENDIX 1. IMAGEJ MACRO FOR AGGREGATE VOLUME MEASUREMENT

```
// Author: Riku Korkiamäki

// Instructions:
// Requires BasiC plugin
// Inside baseDataPath, data needs to be saved in folder named "Aggregate data", and the different genotypes in folders named after the genotype
// Output data is saved in baseDataPath, to a folder "Data", this needs to be created before running script.
// Change process_all = true to process all data in the folder. If false, the script prompts user to continue after each file.

// set to true to hide image windows
// setBatchMode(true);
run("Bio-Formats Macro Extensions");
process_all = true

// Define the base directories
baseDataPath = " ";
testDataPath = baseDataPath + "Aggregate data/";

// Get the list of items (files and folders) in the test data directory
listItems = getFileList(testDataPath);

// Loop through each item in the test data directory
for (i = 0; i < lengthOf(listItems); i++) {
   item = listItems[i];

   // Check if the item is a directory
   isDir = File.isDirectory(testDataPath + item);

   if (isDir) {
      // Treat the item as a folder
      sampleFolderName = item;

      // Create new folder paths
      newFolderPath = baseDataPath + "Output data/" + sampleFolderName;

      // Create the new folder
      File.makeDirectory(newFolderPath);

      // Get the list of files in the current sample folder
      sampleFiles = getFileList(testDataPath + sampleFolderName);

      // Loop through each file in the sample folder
            for (j = 0; j < lengthOf(sampleFiles); j++) {
                  sampleFileName = sampleFiles[j];

                  // Open the sample file
```

```
Ext.openImagePlus(testDataPath + sampleFolderName + "/" +
sampleFileName);

print(sampleFileName);

rename(sampleFileName);

// Initialize variables based on the opened image
original = getTitle();
run("Duplicate...", "duplicate");
wait(100);
title = getTitle();

// Remove the .nd2 suffix from the title for saving path
savingTitle = replace(title, "-1.nd2", "");

// Create a new subfolder for this specific sample file
specificSampleFolderPath = newFolderPath + "/" + savingTitle;
File.makeDirectory(specificSampleFolderPath);

// Update the Thresholded ROIs folder path to be inside the
    new subfolder
thresholdedROIsFolderPath = specificSampleFolderPath +
"/Thresholded ROIs";
File.makeDirectory(thresholdedROIsFolderPath);

// Save the original file in the new subfolder
savePath = specificSampleFolderPath + "/" + savingTitle + ".tif";
saveAs("Tiff", savePath);

// Close the duplicate image
close();

// Re-select the original image for the next operations
selectImage(original);
run("Duplicate...", "duplicate channels=2");
wait(100);


Stack.getPosition(channel, slice, frame);
getVoxelSize(width, height, depth, unit);

run("Select None");

index = 0;
Volume = 0;
rowNumber = 0;
ROI_Zlower = newArray(0); //Array for ROI z-slices
ROI_Zhigher = newArray(0); //Array for ROI z-slices
aggregateArray = newArray(1000);

// Initialize ROI Manager
if (roiManager("count") == -1) {
    run("ROI Manager...");
```

```
}
roiManager("Reset");

selectImage(title);
run("8-bit");

run("BaSiC ", "processing_stack=["+title+"] flat-field=None
dark-field=None shading_estimation=[Estimate shading
profiles] shading_model=[Estimate both flat-field and dark
field] setting_regularisationparametes=Automatic
temporal_drift=[Replace with temporal mean]
correction_options=[Compute shading and correct images]
lambda_flat=0.50 lambda_dark=0.50");

selectImage("Basefluor");
close();
selectImage("Dark-field:"+title);
close();
selectImage("Flat-field:"+title);
close();

selectImage("Corrected:"+title);
run("8-bit");
setVoxelSize(width, height, depth, unit);
run("Maximum 3D...", "x=4.5 y=4.5 z=1.5");
run("Extended Min & Max 3D", "operation=[Extended Maxima]
dynamic=50 connectivity=6");

run("3D OC Options", "volume centroid
mean_distance_to_surface centre_of_mass bounding_box
close_original_images_while_processing_(saves_memory)
dots_size=5 font_size=16 show_numbers white_numbers
redirect_to=none");

run("3D Objects Counter", "threshold=128 slice=18 min.=400
max.=37748736 exclude_objects_on_edges objects statistics");

setMinAndMax(0, 1);
run("Apply LUT", "stack");
getDimensions(width, height, channels, slices, frames);
setSlice(floor(slices/2));

//Reset Log
if (isOpen("Log")){
    selectWindow("Log");
    run("Close");
}

if (nResults > 0) {
// Loop through each row in the "Results" table
for (k = 0; k < nResults; k++) {
     roiWidth = getResult("B-width", k)+40;
     roiHeight = getResult("B-height", k)+40;
     xCorner = getResult("BX", k)-20;
     yCorner = getResult("BY", k)-20;
```

```
        z = floor(getResult("Z", k));
        //+1 slice for both ends
        zlower = floor(z - 3 - (getResult("B-depth", k) / 2));
        zhigher = floor(z + 4 + (getResult("B-depth", k) / 2));
       ROInum = k + 1;

       if(zlower <= 1){
         ROI_Zlower[k] = 1;
       } else {
         ROI_Zlower[k] = zlower;
       }

       if(zhigher >= slices){
          ROI_Zhigher[k] = slices;
       } else {
          ROI_Zhigher[k] = zhigher;
       }

       // Print the slice numbers where the ROI is
       print("ROI_" + ROInum + " slices "+ROI_Zlower[k]+"
       "+ROI_Zhigher[k]);

       // Calculate the top-left corner of the ROI box
       run("Specify...", "width="+roiWidth+" height="+roiHeight+"
       x="+xCorner+" y="+yCorner+" slice="+z+"");
       roiManager("Add");

       // Select the last added ROI
       roiManager("select", k);

       // Rename the ROI with the running number
       roiManager("Rename", "ROI_" + ROInum);
}
selectWindow("Log");
saveAs("Text", specificSampleFolderPath + "/" + savingTitle +
"_slices.txt");
selectWindow("Temporal components");
close();

selectImage("Corrected:"+title);
close();
roiManager("Show All with labels");
run("Clear Results");

//Reset Log table for volume measurements
selectWindow("Log");
run("Close");

// Get the number of ROIs in the ROI Manager
n = roiManager("count");

// Loop through all ROIs in the ROI Manager
for (var m = 0; m < n; m++) {
     run("Clear Results");
     selectImage(title);
```

```
roiManager("Select", m);
                if (isOpen("duplicateforthreshold")) {
                close("duplicateforthreshold");
                }
Stack.getPosition(channel, slice, frame);

ROInumber = m + 1;

selectImage(title);
run("Duplicate...", "title=duplicateforthreshold duplicate
range="+ROI_Zlower[index]+"-"+ROI_Zhigher[index]+"");
selectImage("duplicateforthreshold");
run("Duplicate...", "duplicate");
getDimensions(width, height, channels, slices, frames);

run("Gaussian Blur 3D...", "x=1 y=1 z=0.33");

run("Auto Threshold", "method=Yen white stack
use_stack_histogram");
saveAs("Tiff", thresholdedROIsFolderPath + "/Thresholded
ROI_"+ROInumber);
run("3D Objects Counter", "slice=15 min.=400
exclude_objects_on_edges statistics");
selectImage("duplicateforthreshold");
run("Z Project...", "projection=[Max Intensity]");
rename("ROI_"+ROInumber);

if (nResults == 1) {
    Volume = getResult("Volume (micron^3)", 0);
    aggregateArray[ROInumber] = 1;
}
if (nResults > 1) {
    Volume = "MultipleObjectsError";
    aggregateArray[ROInumber] = 2;
}
if (nResults < 1) {
   Volume = NaN;
   aggregateArray[ROInumber] = 0;
}

print(Volume);
index++;

}

selectWindow("duplicateforthreshold");
close();

roiManager("List");

if (n > 1) {
run("Images to Stack", "name=MontageStack title=ROI_ use");
getDimensions(width, height, channels, slicesMontage, frames);
}
```

```
    if (n == 1) {
    selectImage("ROI_1");
    rename("MontageStack");
    getDimensions(width, height, channels, slices, frames);
    slicesMontage = 1;
    }

    montageselectionWidth = width - 20;
    montageselectionHeight = height - 20;
    rowsMontage = Math.ceil(slicesMontage / 5);
    run("RGB Color");

    // Draws color coded selection on montage slices
    for (p = 0; p < slicesMontage; p++) {

        currentslice = p + 1;
        run("Specify...", "width="+montageselectionWidth+"
        height="+montageselectionHeight+" x=10 y=10
        slice="+currentslice+"");

        if (aggregateArray[currentslice] == 1) {
        setForegroundColor(0, 255, 0);
        run("Draw", "slice");
        }
        if (aggregateArray[currentslice] == 2) {
        setForegroundColor(255, 255, 0);
        run("Draw", "slice");
        }
    }

    if (n > 1) {
    run("Make Montage...", "columns=5 rows="+rowsMontage+"
    scale=1 label");
    } else {
        rename("Montage");
    }

    // Save files
    selectImage("Montage");
    saveAs("Tiff", specificSampleFolderPath + "/" + savingTitle +
    "_Montage.tif");
    selectWindow("Log");
    saveAs("Text", specificSampleFolderPath + "/" + savingTitle +
    "_volumes.txt");
    selectWindow("Overlay Elements of ROI_"+slicesMontage);
    saveAs("Text", specificSampleFolderPath + "/" + savingTitle +
    "_ROI_info.txt");
    close(savingTitle+"_ROI_info.txt");

    roiManager("Save", specificSampleFolderPath + "/" + savingTitle
    + "_RoiSet.zip");

} else {
    print("No ROIs detected");
    selectWindow("Log");
```

```
                                saveAs("Text", specificSampleFolderPath + "/" + savingTitle +
                                "_volumes.txt");
                                }

                        close("*");
                if(process_all == false){
                waitForUser;
                }

                }
        }
}
```

APPENDIX 2. IMAGEJ MACRO FOR ROUNDNESS MEASUREMENT

```
// Author: Kerttu Kotala
// Date: 26.3.2024

// This ImageJ Fiji macro script measures the roundness (and other parameters) of thresholded ROIs of aggregate data.

// Define the base directories
baseDataPath = " ";
outputDataPath = baseDataPath + "Output data/";
codedDataPath = baseDataPath + "Coded data/";

// Get the list of genotypes (files and folders) in the Output data directory
listGenotypesInOutput = getFileList(outputDataPath);

// Print the future column names in .csv format
print("Group,Sample,ROI,Area,XM,YM,Perimetry,Circularity,AR,Roundness,Solidity");

// Loop through each genotype in the Output data directory
for (u = 0; u < lengthOf(listGenotypesInOutput); u++) {
   genotype = listGenotypesInOutput[u];

   // Check if the item is in Output data directory
   isDirOutput = File.isDirectory(outputDataPath + genotype);

   if (isDirOutput) {
      // Treat the item as a genotype folder
      genotypeFolderName = genotype;

      // Get the list of sample (files and) directories in the current genotype folder
      sampleFiles = getFileList(outputDataPath + genotype);

      // Loop through each item in the current sample folder
      for (i = 0; i < lengthOf(sampleFiles); i++) {
                  sample = sampleFiles[i];

                  // Check if the item is a genotype sample directory
                  isDirGenotypeSample = File.isDirectory(outputDataPath + genotype + sample);

                  if (isDirGenotypeSample) {

                  sampleFolderName = sample;

                  thresholdedROIspath = outputDataPath + genotypeFolderName +
                  sampleFolderName + "Thresholded ROIs/";

                  ROIlist = getFileList(thresholdedROIspath);

                  // Loop through all ROIs of one sample and perform the analysis for them
                  for (a = 0; a < lengthOf(ROIlist); a++) {
                              individualROI = ROIlist[a];
```

```
imageToBeSelected = thresholdedROIspath + individualROI;
open(imageToBeSelected);

// Z-projection
run("Z Project...", "projection=[Max Intensity]");

// Define the middle of the image in µm
pixel_size = 0.0985018;
getDimensions(width, height, channels, slices, frames);
width_um = width * pixel_size;
height_um = height * pixel_size;

ROI_x_middle = width_um / 2;
ROI_y_middle = height_um / 2;

// Invert
run("Invert");

// Parameter measurement
run("Set Measurements...", "area center perimeter shape
redirect=None decimal=5");

run("Analyze Particles...", "size=1-Infinity unit show=Nothing
display clear overlay");

// Close images
close("*");

// Preparations for the next loop
results_rows = getValue("results.count");
closestRowIndex = -1;
minDistance = 999999;

// If there are any results in the Results table, the following
functions are applied. If not, the Results table is not considered at
all.
if (results_rows > 0 ) {
   // Loop through the rows in the Results table to define the
   particle in the middle
   for (r = 0; r < results_rows; r++) {
        // Retrive the X and Y values of the current row
        x_value_um = getResult("XM", r);
        y_value_um = getResult("YM", r);

        // Calculate the distance from the current point to the
        middle of the ROI
        distance = sqrt(pow(x_value_um - ROI_x_middle, 2) +
        pow(y_value_um - ROI_y_middle, 2));

        // If the current distance is less than the smallest found so
        far, update the closest row and minimum distance
        if (distance < minDistance) {
                minDistance = distance;
                closestRowIndex = r;
        }
```

```
                        }

                        // Get the analysis results of the particle in the middle from the
                        Results table

                        // If more than one area was detected
                        if (results_rows > 1){
                           area = getResult("Area", closestRowIndex);
                           XM = getResult("XM", closestRowIndex);
                           YM = getResult("YM", closestRowIndex);
                           perimetry = getResult("Perim.", closestRowIndex);
                           circularity = getResult("Circ.", closestRowIndex);
                           AR = getResult("AR", closestRowIndex);
                           roundness = getResult("Round", closestRowIndex);
                           solidity = getResult("Solidity", closestRowIndex);
                        }

                        // If only one area was detected
                        if (results_rows == 1) {
                           area = getResult("Area", 0);
                           XM = getResult("XM", 0);
                           YM = getResult("YM", 0);
                           perimetry = getResult("Perim.", 0);
                           circularity = getResult("Circ.", 0);
                           AR = getResult("AR", 0);
                           roundness = getResult("Round", 0);
                           solidity = getResult("Solidity", 0);
                        }

                        // Exctract group, sample, and ROI names
                        groupName = replace(genotype, "/", "");
                        sampleName = replace(sample, "/", "");
                        ROIName = a + 1;

                        // Print the results in log window in .csv format
                        print(groupName + "," + sampleName + "," + ROIName + "," +
                        area + "," + XM + "," + YM + "," + perimetry + "," + circularity + ","
                        + AR + "," + roundness + "," + circularity);

                }

                }

                }

        }

        }
}

selectWindow("Log");
saveAs("Text", codedDataPath);
```